Accepted Article

Microstructure Evolution of Organic Matter and Clay Minerals in Shales with Increasing Thermal Maturity

GU Yuantao[1, 2], LI Xiaoxia[1], YANG Shuguang[2], and WAN Quan[2, *]

[1] *School of resource and environment, Henan University of Engineering, Zhengzhou 451191, Henan, China*

[2] *State Key Laboratory of Ore Deposit Geochemistry, Institute of Geochemistry, Chinese Academy of Sciences, Guiyang 550081, Guizhou, China*

Abstract: As the two important components of shale, organic matter (OM) and clay minerals are usually thought to strongly influence the hydrocarbon generation, enrichment and exploitation. The evolution process of OM and clay minerals as well as their interrelationship over a wide range of thermal maturities are not completely clear. Taking Yanchang (T_3y), Longmaxi (S_1l) and Niutitang ($Є_1n$) shales as examples, we have studied the microstructure characteristics of OM and clay minerals in shales with different thermal maturities. The effects of clay minerals and OM on pores were reinforced through sedimentation experiments. Using a combination of field emission scanning electron microscopy (FE-SEM) and low-pressure N_2 adsorption, we investigated the microstructure differences among the three shales. The results showed that both OM and clay minerals have strong effects on pores, and small mesopore (2–20 nm) is the dominant pore component for all three samples. However, the differences between the three samples are embodied in the distribution of pore size and the location. For the T_3y shale, clay minerals are loosely arranged and develop large amounts of pores, and fine OM grains often fill in intergranular minerals or fractures. Widespread OM pores distribute irregularly in S_1l shale, and most of the pores are elliptical and nondirectional. The $Є_1n$ shale is characterized by the preferred orientational OM-clay aggregates, and lots of pores in the composites are in the mesopore range, suggesting that over maturity lead to the collapse and compaction of pores under huge pressure of strata. The results of the current research imply that with increasing thermal maturity, OM pores are absent at low maturity (T_3y), are maximized at high maturity (S_1l) and are destroyed or compacted at over-mature stage ($Є_1n$). Meanwhile, clay minerals have gone through mineral transformation and orientational evolution. The interaction of the two processes makes a significant difference to the microstructure evolution of OM and clay minerals in shale, and the findings provide scientific foundation in better understanding diagenetic evolution and hydrocarbon generation of shale.

Key words: organic matter, clay minerals, OM-clay composites, microstructure evolution, thermal maturity

Email: wanquan@vip.gyig.ac.cn

1. Introduction

This article has been accepted for publication and undergone full peer review but has not been through the copyediting, typesetting, pagination and proofreading process, which may lead to differences between this version and the Version of Record. Please cite this article as doi: 10.1111/1755-6724.14285.

This article is protected by copyright. All rights reserved.

Accepted Article

Shales are heterogeneous rocks with variations in structure and composition existing on many levels, from the nanoscale up to the macroscale (Curtis et al., 2012; Bernard and Horsfield, 2014). For most shales, organic matter (OM) and clay minerals, as the two important components of shale, play an important role in hydrocarbon generation, enrichment and exploitation. The microstructure can differ dramatically between shale plays and even within the same play (Curtis et al., 2010, 2012). Understanding how microstructure develops in OM and clay minerals is essential for predicting the storage and production capacity of hydrocarbons in shales (Kuila et al., 2014). Thermal maturity (R_o), to a certain extent, is a representative parameter to estimate the evolutionary history of shale. Therefore, the important thing in determining the potential of a shale to produce hydrocarbons is knowing the thermal maturity of the shale (Curtis et al., 2012). Many previous studies have been performed on natural samples with different thermal maturities or artificially mature samples by pyrolysis experiments (Curtis et al., 2012; Chen and Xiao, 2014; Kuila et al., 2014; Romero-Sarmiento et al., 2014; Tang et al., 2015). For example, Curtis et al. (2012) investigated the organic porosity within Woodford Shale samples with vitrinite reflectance values ranging from 0.51 % to 6.36 %, and thought that maturity alone was not a reliable predictor of porosity in OM and other factors (such as OM composition) complicate this predication. Chen and Xiao (2014) analyzed nanopores characteristics of artificial shale samples across a maturation gradient by laboratory anhydrous pyrolysis and roughly subdivided evolution of the OM nanopores in shales into three stages: formation stage, development stage, and conversion or destruction stage. However, the evolution of OM and clay minerals as well as their interrelationship over a wide range of thermal maturities have not been thoroughly explored.

In the present study, three representative shales with different maturities in China, i.e., Yanchang (T_3y) shale, Longmaxi (S_1l) shale and Niutitang ($Є_1n$) shale, were collected to investigate the microstructure characteristics of OM and clay minerals. The successful finding of industrial gas flow in T_3y has demonstrated the great potential of Ordos Basin (Guo et al., 2014; Dong et al. 2016). S_1l shale has been verified as a most commercially valuable shale gas reservoir in China. The S_1l shale, mostly distributed in the Sichuan Basin, has been exploited commercially in the Jiaoshiba shale gas field (Tan et al., 2015), with cumulative production from this formation exceeding 60×10^8 m^3 in 2015 (Dong et al. 2016). The $Є_1n$ shale, widely developed in the Upper Yantze platform, has been considered a promising shale gas reservoir (Lu et al., 2015; Dong et al. 2016; Wang et al., 2016). The three shales (T_3y, S_1l, $Є_1n$) represent low maturity (0.5–1.2 %), high-over maturity (2.0–3.2 %), and over maturity (3.0–5.0 %), respectively (Er et al., 2013; Dong et al. 2016). Taking the three shales as examples, this study examined the microstructure evolution of OM and clay minerals in shale using low pressure N_2 adsorption and field emission-scanning electron microscopy (FE-SEM). Based on our results, we assessed the evolutionary pattern of OM and clay minerals with increasing thermal maturity, which would make a big difference in predicting the potential productivity of hydrocarbons in shales and provide scientific foundation for understanding the diagenetic evolution and hydrocarbon generation of shale.

2. Geological Setting

Previous studies have proved that the $Є_1n$ and S_1l shales were deposited under an epicontinental sea sedimentary environment (Liang et al., 2009). The lower strata of the $Є_1n$ and S_1l shales, as the main production layer of shale gas, are in a deep-water shelf environment (Lu et al., 2015; Yang et al., 2012; Zhang et al., 2012; Zhao et al., 2016), in which real advantages were provided for the formation of shale gas reservoirs by the high contents of silica and OM. As a typical continental shale in Ordos Basin, the T_3y shale was deposited in silent deep lake, which was favorable for the development of organic-rich shale (Yuan et al., 2015).

The regional geology of the two basins is shown in Fig. 1. The Sichuan Basin is located at the transition zone between the Paleo-Pacific Tectonic Domain and the Tethys-Himalayan Tectonic

This article is protected by copyright. All rights reserved.

Accepted Article

Domain. The marine shales distributed in the Sichuan Basin have experienced substantial burial (high thermal maturation), significant uplift and erosion, and strong deformation from Mesozoic to Cenozoic (Liu et al., 2016). Around Sichuan Basin (Fig. 1a), Longmenshan and Dabashan thrust belts are distributed along with the northwest and northeast boundary of the basin, respectively, and Emei-Liangshan and Xiang-Qian-E fold belts are distributed at the southwest and southeast of the basin. In this study, the S_1l shale sample was collected from the southern end of Sichuan Basin, and the $Є_1n$ shale sample was obtained at the Xiang-Qian-E fold belt.

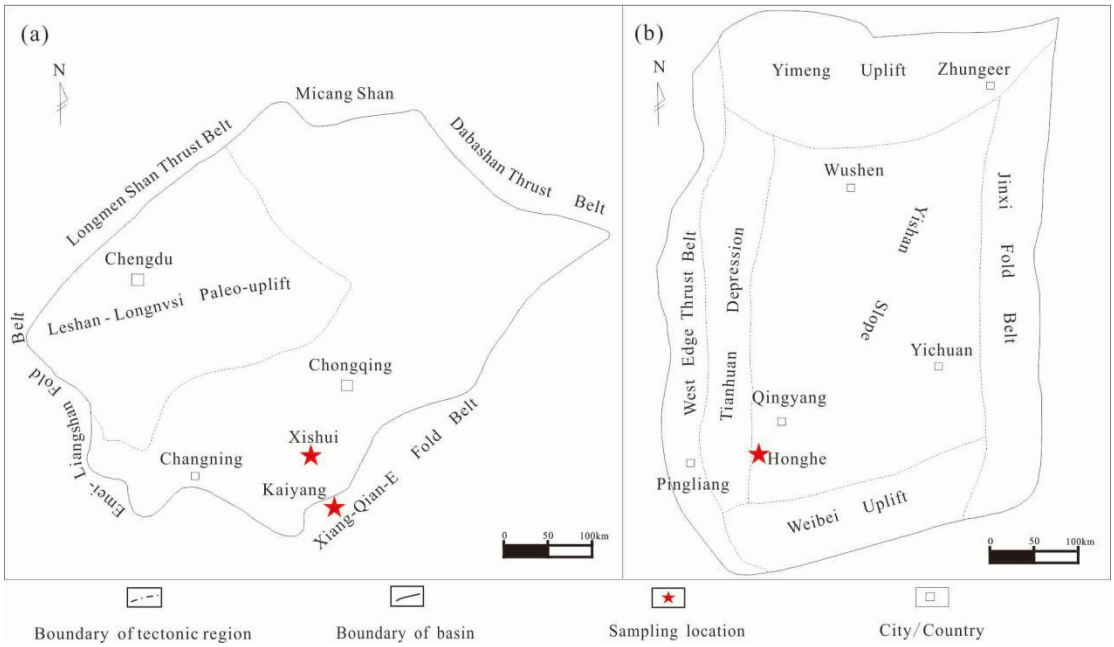

Fig. 1. The location of the sampling sites and the regional geology of Sichuan Basin (a) and Ordos Basin (b).

The Ordos Basin, located in northern-central China, is the second largest sedimentary basin in China, with vast oil and gas reserves (Dai et al., 2005; Duan et al., 2008; Yang et al., 2016b). The Ordos Basin is an intracratonic depression basin and one of the most tectonically stable basins in China (Dai et al., 2005; Guo et al., 2014). Six major structural units, including the Yimeng uplift in the north, the Weibei uplift in the south, the Tianhuan depression and Western edge thrust belt in the west, the Jinxi fold belt in the east, and the central Yishan slope (Fig. 1b) (Duan et al., 2008; Guo et al., 2014), compose the basin. The T_3y shale used in this paper was sampled from the southwest edge of the Yishan slope, which is the main oil and gas exploitation area in the basin (Dai et al., 2005; Guo et al., 2014).

3. Samples and methods

3.1 Samples

Three samples from economically valuable source rocks were collected from a borehole to carry out this research. The first was collected from the continental shale of T_3y in Honghe-2 well, Ordos Basin, China. The second sample was mined at a depth of several meters from a shallow hole of S_1l in Xishui, Guizhou Province. The last sample was obtained from a drill of $Є_1n$ in Kaiyang, Guizhou Province. The location of the three sampling sites can be seen in Fig. 1.

This article is protected by copyright. All rights reserved.

Accepted Article

3.2 Sedimentation Experiments

To magnify the effects of OM and clay minerals on pore characteristics, sedimentation experiments were performed on the three samples. First, the three samples were crushed and ground to 200 mesh, and we called the powder primary samples. Then, we weighed a 5-g powdered sample into a beaker and added deionized water to soak the powder. All the samples were agitated and ultrasonicated to disperse the powder adequately. According to the Stokes sedimentation laws, the clay-sized was allowed to stand for 8 h, and the upper layer of the clay-sized (10 cm) was then extracted via siphon. After the extraction, an amount of deionized water equal to the amount above was added to the beaker, and the agitation and resting procedure was repeated twice. Next, the extracted clay-sized layer was centrifuged at 7000 r/min to remove the water, and then the solid was dried in an oven at 40 °C (Ding et al., 2013). After being dried, the powder samples, which we called clay-sized samples, were ready for use in the next test. TOC content, mineralogical composition and low-pressure N_2 adsorption were performed on the primary samples and the clay-sized samples.

3.3 Organic Geochemical Analyses

The TOC of all samples was measured using a vario MACRO cube organic element analyzer following the Chinese Oil and Gas Industry Standard GB/T19145-2003. Before the measurement was taken, inorganic carbon in the samples was eliminated by the addition of diluted hydrochloric acid at a ratio of HCl: H_2O = 1:7 (V/V). The measurements were performed at State Key Laboratory of Environmental Geochemistry, Institute of Geochemistry, Chinese Academy of Sciences

Previous researches on thermal maturity have indicated that laser Raman spectroscopy is a suitable method to calculate the reflectance (Chen et al., 2015; David, 2013; Kelemen and Fang, 2001). A Renishaw Invia Reflex Laser Raman Spectrometer at State Key Laboratory of Ore Deposit Geochemistry, Institute of Geochemistry, Chinese Academy of Sciences was used to measure the reflectance values of the three shales. In this work, the calculation of reflectance values (R) follows the equation: R = 0.0537 d (G-D)-11.21, where G, D, and d(G-D) denote peak positions of the graphitic carbon and disordered carbon and the interpeak intervals between G and D, respectively (Kelemen and Fang, 2001; Liu et al., 2012). For T_3y, the R represents vitrinite reflectance (R_o), while for S_1l and $Є_1$n shales, due to the absence of vitrinite in the Lower Paleozoic marine shale, the bitumen reflectance (R_b) was measured to identify thermal maturity of samples. The relation $R_o = (R_b+0.2443)/1.0495$ is used to calculate R_o, according to the relationship between R_b and R_o (Schoenherr et al., 2007).

3.4 Mineralogical Composition

A PANalytical Empyrean X-ray diffractometer (XRD) was used to determine the mineralogical composition of the samples. The testing angle ranged from 5° to 80°. The results were analyzed quantitatively following the Chinese Oil and Gas Industry Standard (SY/T) 5163-2010. The tests were conducted at State Key Laboratory of Ore Deposit Geochemistry, Institute of Geochemistry, Chinese Academy of Sciences.

3.5 FE-SEM

Before the SEM observation, all samples were polished by a Technoorg SC1000 argon ion polisher operated at an 8-kV acceleration voltage to obtain a smooth surface. Then, the samples were sputter coated with gold. An FEI Scios FE-SEM at Center for Lunar and Planetary Sciences, Institute of Geochemistry, Chinese Academy of Sciences was used to characterize the distribution of nanoscale pores in shale samples.

This article is protected by copyright. All rights reserved.

Accepted Article

3.6 Low-pressure N_2 Adsorption

Low-pressure N_2 adsorption experiments were performed on a Quantachrome Autosorb-iQ_2 automatic gas absorption analyzer at State Key Laboratory of Ore Deposit Geochemistry, Institute of Geochemistry, Chinese Academy of Sciences. To remove the free water and small amounts of volatile impurities, all samples were outgassed at 150 °C for 4 hours before adsorption measurements. The N_2 adsorption isotherms were obtained at 77 K (-196 °C), and the relative pressure (p/p_0) ranged from 10^{-6} to 0.99. The specific surface area (S_{BET}) was calculated using the multipoint Brunauer-Emmett-Teller (BET) method. The pore volume was acquired using the nonlocal density functional theory (NLDFT).

4. Results

4.1 Composition Characteristics

The TOC, R_o and mineralogical composition of the three samples are shown in Table 1. TOC contents of these samples was 4.3 % in T_3y, 4.8 % in S_1l, and 5.6 % in $Є_1n$, which suggests that all the three samples are organic-rich shale (>2.0 %). T_3y is immature source rock entering the oil window (1.1 % R_o) whereas S_1l and $Є_1n$ are in the gas window (2.4–3.3 % R_o). Various proportions of silicates (quartz, feldspar, and clay minerals), and sulfur-bearing minerals (pyrites) were evidenced from powder XRD. The overall mineralogical compositions were dominated by quartz, clay minerals (including illite, kaolinite and smectite), and feldspar. The presence of pyrite indicates that sulfate reduction took place in lacustrine (T_3y) or marine facies (S_1l and $Є_1n$).

Table 1. The burial depth, TOC, R_o and mineralogical composition of the three samples

Sample ID	Burial Depth (m)	R_o (%)	TOC (%)	Quartz (%)	Illite (%)	Kaolinite (%)	Smectite (%)	Feldspar (%)	Pyrite (%)	Calcite (%)	Dolomite (%)
T_3y	940.0	1.1	4.3	59.8	6.8	10.5	1.9	12.7	8.3	nd	nd
S_1l	5.0	2.4	4.8	37.2	17.3	6.2	nd	18.4	2.2	5.6	3.7
$Є_1n$	964.5	3.3	5.6	36.4	24.1	12.1	nd	16.0	3.3	nd	8.1

Note: nd = not detected

To evaluate nanoscale pore size distribution in clay minerals and OM deeply, sedimentation experiments were performed to extract clay minerals and OM. The TOC and mineralogical composition of the clay-sized samples were also tested (Table 2). The TOC values of the clay-sized samples were greater than those of the corresponding primary samples because of the low density of OM. For all the three samples, the clay mineral contents of the clay-sized samples, principally for illite, were generally much greater than that of the primary samples. For the brittle minerals (quartz, feldspar, calcite, and dolomite), things just go opposite, i.e., brittle mineral contents of the clay-sized samples were generally less than that of the primary samples. The differences in mineralogical composition between the primary samples and the clay-sized samples should be caused by the smaller particle size and the lower density of the clay mineral content relative to the brittle minerals.

Table 2. The TOC and mineralogical composition of the clay-sized samples

This article is protected by copyright. All rights reserved.

Accepted Article

Sample ID	TOC (%)	Quartz (%)	Illite (%)	Kaolinite (%)	Smectite (%)	Feldspar (%)	Pyrite (%)	Calcite (%)	Dolomite (%)
T_3y	5.8	40.8	17.9	16.4	5.2	16.8	2.9	nd	nd
S_1l	6.4	37.8	37.1	6.5	nd	6.8	2.1	2.3	2.1
$Є_1n$	7.7	16.9	55.3	13.5	nd	7.3	3.3	nd	2.4

Note: nd = not detected

4.2 Adsorption Characteristics

Low-pressure N_2 adsorption, as one of the most common techniques used to characterize nanoscale pore structures for shale, can provide a reliable assessment of the surface area, pore volume and pore size distribution (PSD). To develop a better understanding of N_2 adsorption behavior on OM and clay minerals in particular, both primary samples and the clay-sized samples were investigated by low-pressure N_2 adsorption and the N_2 adsorption isotherms are shown in Fig. 2. The isotherms of all samples can be classified as Type IIb according to a refined International Union of Pure and Applied Chemistry (IUPAC) grouping method (Rouquerol et al., 1994; Sing et al., 1985). The micropore (<2 nm) filled by nitrogen molecules at extremely low relative pressure (P/P_0<0.01) results in the sharp increase in the adsorption volume. The monolayer-multilayer adsorption on mesopore (2–50 nm) walls occurs at intermediate P/P_0. The absence of a plateau (as in mesoporous Type IV isotherms) and a steep slope in the P/P_0 range of 0.98–1.00 result from the existence of macropores (>50 nm) (Rouquerol et al., 1994). All the T_3y and S_1l samples exhibit a hysteresis behavior, which shows the existence of mesopores, and the $Є_1n$ samples present an inconspicuous type H3 hysteresis loop. This isotherm type and hysteresis loop shape indicate that our samples contain aggregates of plate-like particles (e.g., clay minerals) and possess nonrigid slit-shaped pores (Rouquerol et al., 1994).

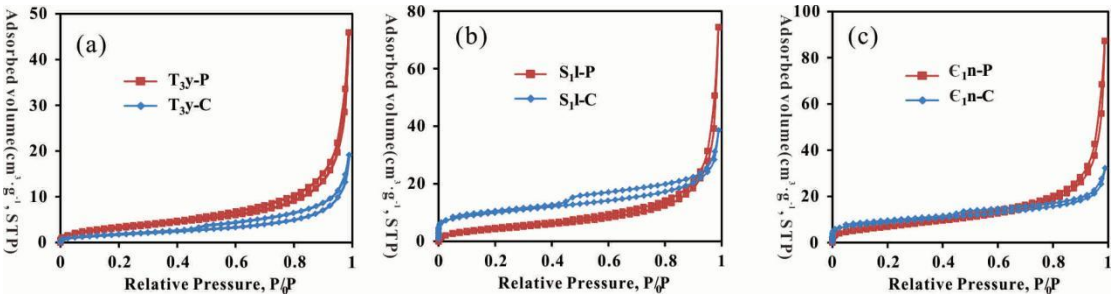

Fig. 2. N_2 adsorption-desorption isotherms of primary samples (P) and clay-sized samples (C).

(a) presents the T_3y shale, (b) presents the S_1l shale, and (c) presents the $Є_1n$ shale.

Like the primary samples, all the clay-sized samples present type IIb isotherms and an inconspicuous type H3 hysteresis loop, which indicates that there is little difference in the pore types between the primary samples and the clay-sized samples. However, there is a large difference in adsorption volume. At low P/P_0 (<0.01), the adsorption volumes of the S_1l shale primary samples are larger than those of the clay-sized samples, while there is no clear difference for theT_3y and $Є_1n$ shale, which may be caused by the difference in the locations (clay or OM) of the micropores and mesopores between S_1l shale and $Є_1n$ shale. The adsorption volumes of the clay-sized samples are much larger than those of the primary samples for all three samples at high P/P_0 (0.98–1.00). The large increase of adsorption volumes at high P/P_0 can be attributed to the abundant macropores (either inherent or artificial pores created by particle packing) in clay-sized samples.

This article is protected by copyright. All rights reserved.

Accepted Article

4.3 Microstructure Characteristics

To further clear the microstructure characteristics of the three shale samples, FE-SEM was used to observe the morphology of clay minerals and OM directly. In the three samples, some common ground structure characteristics are illustrated by Fig. 3, Fig. 4 and Fig. 5. First, OM and clay minerals are easily found in the three samples, indicating that both are indispensable in the generation, storage, and seepage of shale gas, though the great disparities of morphology exist among the three samples. Second, partial pyrite grains coexist with OM (Fig. 3a, c; Fig. 4a, c, f; Fig. 5a, b, d), which may be because both pyrite and OM prefer a reducing sedimentary environment. Last but not least, microfractures can be found between mineral grains and/or OM grains (Fig. 3a, c; Fig. 4b–d; Fig. 5a, e), which could have very important effects on the storage and permeable migration of shale gas (Hartman et al., 2011; Slatt and O'Brien, 2011; Ding et al., 2012; Dong et al., 2018).

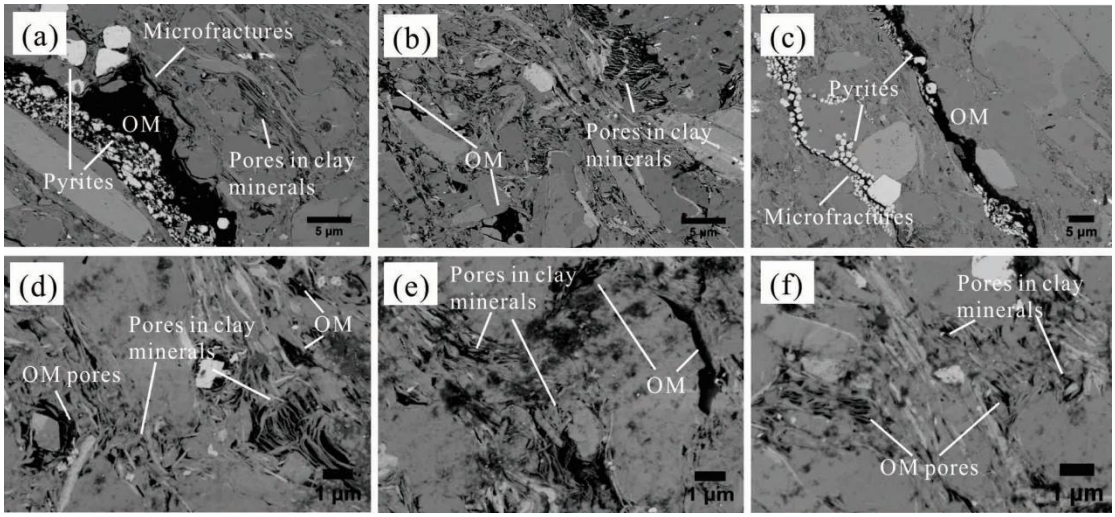

Fig. 3. FE-SEM images for the T_3y shale.

(a) , (b) and (d)–(f) present the well-developed pores in clay minerals; (a) and (c) illustrate the coexistence of OM and pyrites, as well as microfractures; (a), (b) and (e) present the non-porous OM.

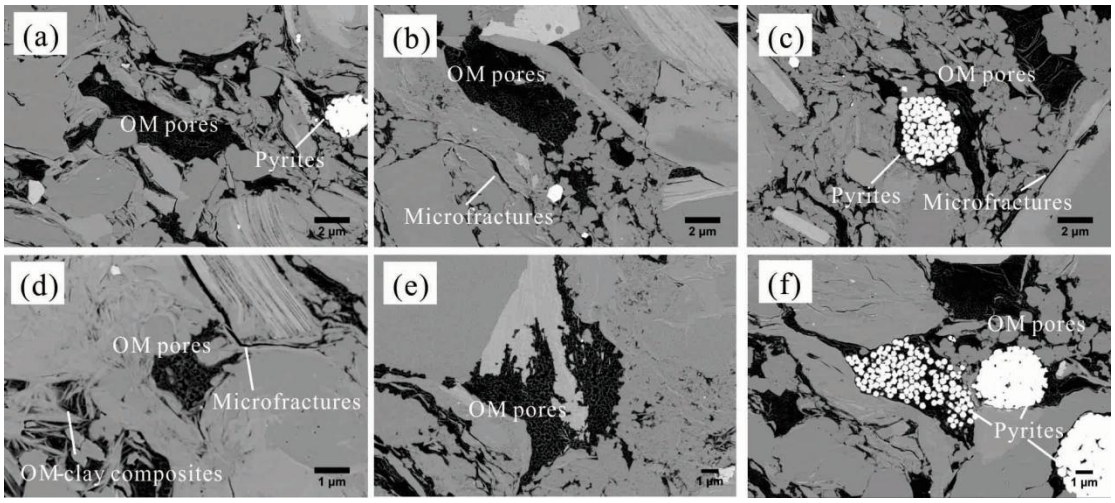

Fig. 4. FE-SEM images for the S_1l shale.

(a)–(f) present the well-developed OM pores; (a), (c) and (f) illustrate the coexistence of OM and pyrites; (b)–(d) present microfractures

This article is protected by copyright. All rights reserved.

between minerals and/or OM grains.

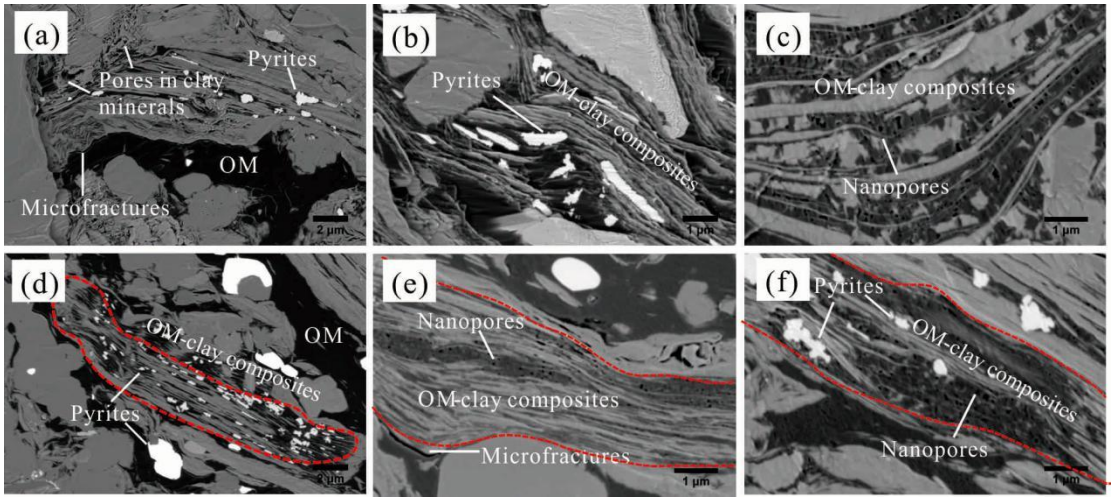

Fig. 5. FE-SEM images for the $Є_1$n shale.

(a) –(f) indicate the exist of OM-clay composites; (c)–(f) present the well-developed pores in OM-clay composites; (a), (b) and (d) illustrate the coexistence of OM and pyrites; (a) and (e) present the microfractures between OM and clay minerals; (d)–(f) illustrate the preferred orientational arrangement of OM-clay composites (in or between the red dashed lines).

Despite all the common characteristics described above, the three samples display a marked difference in pore distribution, morphological characteristics, and the relationship of OM and clay minerals. Fig. 3 shows the microstructure characteristics of the T_3y shale, which is characterized by widely developed interparticle pores in clay minerals and microfractures. Most of the microfractures are filled with pyrite crystallites and organic matter (Fig. 3a, c), indicating the reducing sedimentary environment and that the microfractures are probably caused by locally abnormal pressure in organic matter evolution (Yang et al., 2016a). Many interparticle pores in clay minerals are linear in shape, whereas some pores have triangular shapes, which are defined by the lattice of randomly oriented clay mineral platelets (Fig. 3a, b, d–f). Most of the pores range between dozens and hundreds of nanometers in diameter. OM pores are not developed and have a much smaller size than the pores in clay minerals (Fig. 3a–e). From Fig. 4, it is easily observed in S_1l shale that almost all of the organic grains with diameters of several micrometers contain innumerable nanopores with various shapes and sizes. The OM pores are various in shape such as ellipsoid, elongated bubble, irregular shape, but ellipsoid is the most common shape, and most of the OM pores lack a preferred orientation (Fig. 4). Several to a few hundred nanometers pores distribute widely in organic grains (Fig. 4), which is very similar to the dimension of OM pores investigated by Loucks et al. (2009, 2012). Fig. 5 presents few OM pores and widely developed interparticle pores in clay minerals and OM-clay composites for $Є_1$n shale. The pores in OM-clay composites are most in several to tens of nanometers (Fig. 5c, e, f). In addition, the composites and OM grains have a preferred orientational arrangement (see the red dashed lines in Fig. 5d–f), which may be attributed to the release of internal overpressure in nanopores and compaction of pores under huge pressure of strata.

5. Discussion

5.1 Pore Distribution Characteristics

The PSD (NLDFT) results for the primary samples and clay-sized samples are shown in Fig. 6. The primary samples are dominated by mesopores for T_3y, and the plots of S_1l and $Є_1$n present a clear

This article is protected by copyright. All rights reserved.

Accepted Article

Accepted Article

bimodality with two peaks near 1 nm and 2–10 nm. Compared to primary samples, micropores are absent in the clay-sized samples of S_1l and C_1n, very likely because during sedimentation of the shale samples, water molecules could occupy sorption sites in the micropores and block the pore throat by dispersed or dissolved clay mineral due to the strong water sensitivity of clay minerals (Chalmers and Bustin, 2007; Ju et al., 2014). The distribution of mesopore and macropore in the clay-sized samples are more obvious than in the primary samples, which indicates that mesopore and macropore are distributed mostly in OM or clay minerals.

In addition, the cumulative pore volume (CPV) curves for the primary samples and clay-sized samples always intersect (Fig. 6), indicating that the pore volumes of primary samples are larger than those of the clay-sized samples when the pore size is less than the intersection value, and when the pore size is greater than the intersection value, the pore volumes of primary samples are lower than those of the clay-sized samples. The intersections for the S_1l shale are larger than 20 nm but smaller than 20 nm for the T_3y and C_1n shales. To quantitatively evaluate PSD characteristics in more detail, according to pore size, the pores can be classified into four types: micropore (<2 nm), small mesopore (2-20 nm), large mesopore (20-50 nm) and macropore (>50 nm).

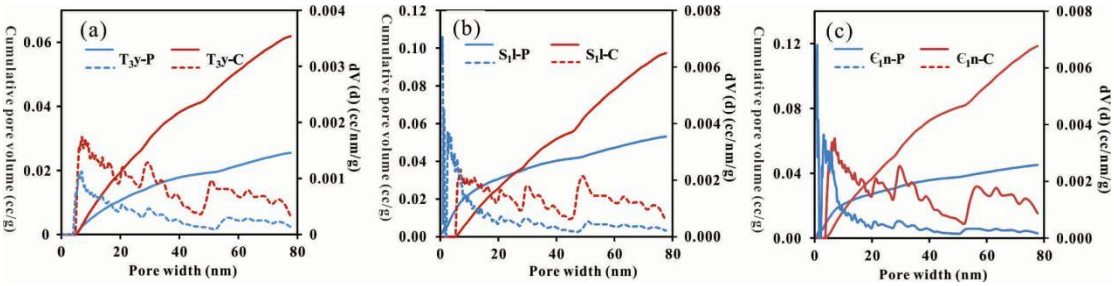

Fig. 6. Pore size distribution of primary samples (P) and clay-sized samples (C) for all samples.

(a) presents the T_3y shale, (b) presents the S_1l shale, and (c) presents the C_1n shale. Solid denotes CPV (cumulative pore volume) curves; Dashed denotes PSD (pore size distribution) curves.

The pore structure parameters of the three samples are presented in Table 3, including specific surface area (S_{BET}), average pore diameter (D_{ave}) and total pore volume (V_{tot}), micropore volume (V_{mic}), small mesopore volume ($V_{2\text{-}20}$), as well as large mesopore volume ($V_{20\text{-}50}$). Among the three samples, the sample T_3y has the lowest S_{BET} and total pore volume (V_{tot}), as well as largest D_{ave}. The S_{BET} and V_{tot} of S_1l and C_1n shales are much larger than that of T_3y, while the D_{ave} of S_1l and C_1n are much less than that of T_3y. The higher TOC contents and R_o of S_1l and C_1n should be responsible for the trend. For all primary samples, D_{ave} (6.7 to 17.0 nm) fell within the small mesopore range, and $V_{2\text{-}20}$ is larger than the other three types of pore (micropore, large mesopore and macropore) volume. Logically, small mesopore is clearly the dominant pore component in the three shale samples.

Table 3. Pore structure parameters of the three samples

Sample ID	S_{BET}[a] (m^2/g)	D_{ave}[b] (nm)	V_{tot}[c] (cm^3/g)	V_{mic}[d] (cm^3/g)	$V_{2\text{-}20}$[e] (cm^3/g)	$V_{20\text{–}50}$[f] (cm^3/g)
T_3y	6.9	17.0	0.025	0	0.011	0.008
S_1l	35.4	6.7	0.053	0.005	0.026	0.012
C_1n	31.3	6.4	0.045	0.004	0.023	0.011

Note: [a]S_{BET} = specific surface area, [b]D_{ave}= average pore diameter, [c]V_{total} = total pore volume, [d]V_{mic} = micropore volume, [e]$V_{2\text{-}20}$ = small mesopore volume, [f]$V_{20\text{-}50}$ = large mesopore volume.

This article is protected by copyright. All rights reserved.

Accepted Article

Table 4 present the six pore structure parameters of the clay-sized samples. For T_3y shale, because of the absence of OM pores (Fig. 3), no micropores can be detected in the sample. In S_1l and $Є_1n$ shales, V_{mic} of the clay-sized samples decreases to 0 cm^3/g, which may be because water molecules could occupy sorption sites in micropores during sedimentation (Chalmers and Bustin, 2007). Fig. 7 illustrates the variation trends of the other five pore structure parameters (S_{BET}, V_{tot}, V_{2-20}, V_{20-50}, and D_{ave}) before and after extraction. Compared with primary samples, D_{ave}, V_{tot} and V_{20-50} of the clay-sized samples have presented apparent increase trends for all the three samples. The S_{BET} and V_{2-20} have exhibited different variation trends for the three shales (Fig. 7). Combining with FE-SEM observation, the differences between T_3y, $Є_1n$ and S_1l suggest the differences of pore distribution regularities in clay minerals and OM. Previous studies have verified that micropore in shale reservoirs are mostly developed in OM, which can be concluded by the strong positive relationship between V_{mic} and OM content, while mesopore and macropore could develop in OM or clay minerals (Chalmers and Bustin, 2007, Chen and Xiao, 2014). Consequently, in contrast with primary samples, the clay-sized samples should have larger specific surface area and pore volume (including V_{tot}, V_{mic}, V_{2-20} and V_{20-50}). For the T_3y shale, the increase in S_{BET}, V_{tot}, V_{2-20} and V_{20-50} should be interpreted as the development of pores in clay minerals (Fig. 3). However, things turned out differently for the S_1l shale. Fig. 4 indicates the predominant control of OM on pores. The S_{BET} and V_{2-20} of the clay-sized sample are much less than those of the primary sample, which may be because of the decrease in V_{mic} and that pore throat in OM could be blocked by dispersed or dissolved clay minerals due to the strong water sensitivity of clay minerals (Chalmers and Bustin, 2007; Ju et al., 2014). For the $Є_1n$ shale, the zeroth V_{mic} also leads to the small decrease in S_{BET}, but V_{2-20} of the clay-sized sample is larger than that of the primary sample because large amounts of small mesopores were found in OM-clay composites and clay minerals (Fig. 5), while the clay layers in OM-clay composites have a more stable laminated structure and are not easily affected by water molecules (Lu et al., 2013), resulting in the pores in OM-clay composites still being detected by nitrogen molecules after extraction. In addition, the increase in D_{ave} should be attributed to three aspects: the blockage of micropores or small mesopores (mainly for S_1l), the considerable development of large mesopore and macropore in OM and clay minerals (Fig. 3, 4, 5), as well as the macropores created manually during extraction.

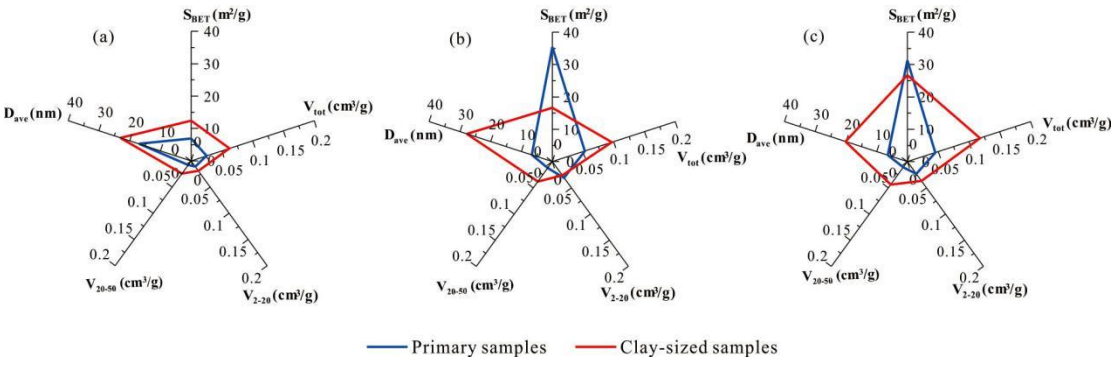

Fig. 7. The variation trends of five pore structure parameters (S_{BET}, V_{tot}, V_{2-20}, V_{20-50}, and D_{ave}) of the three samples before and after extraction.

(a) presents the T_3y shale, (b) presents the S_1l shale, and (c) presents the $Є_1n$ shale. Blue lines denote the primary samples, and red lines denote the clay-sized samples

Table 4. Pore structure parameters of clay-sized samples

Sample ID	S_{BET}[a] (m^2/g)	D_{ave} (nm)	V_{total} (cm^3/g)	V_{mic} (cm^3/g)	V_{2-20} (cm^3/g)	V_{20-50} (cm^3/g)

This article is protected by copyright. All rights reserved.

Accepted Article

T_3y	12.4	23.0	0.062	0	0.019	0.024
S_1l	16.6	27.8	0.097	0	0.025	0.038
$Є_1n$	26.7	20.2	0.118	0	0.037	0.044

5.2 The Evolution of OM and Clay Minerals

The strong correlation between nanopore abundance in grains of OM and R_o has been proved in previous studies, suggesting that pore formation is the result of thermal maturation and conversion of OM (i.e., kerogen). This conclusion is supported by the abundance of nanopores in more thermally mature samples and the absence in OM grains from our lower thermal maturity samples (Loucks et al., 2007). However, when OM in shale evolves into over maturity, transformation and destruction of OM pores will occur. For example, Chen and Xiao (2014) analyzed the evolution process of nanoporosity in organic-rich shales during thermal maturation by conducting anhydrous pyrolysis experiments on shale samples and found that OM pores are enlarged after R_o>3.5 %, with a decrease of V_{mic}, which can be attributed to the transformation of micropores to mesopores and/or macropores. For our three samples, OM pores are absent at low maturity (T_3y) and reach the peak at high maturity (S_1l) and are destroyed or compacted at over-mature stage ($Є_1n$) (Fig. 3, 4, 5), which implies that OM pore abundance is positive correlated with thermal maturity before the sample reaches high maturity, and then OM pores are destructed with further increasing thermal maturity. This evolutionary process is consistent with the study of Chen and Xiao (2014), i.e., in the formation and development stage, thermal maturation and conversion of OM could result in OM pores being more and more developed with increasing thermal maturity (from Fig. 3 to Fig. 4), while in the conversion or destruction stage, due to the carbonization and compaction of OM, a progressive decline happens to OM pores with further increase of maturity (from Fig. 4 to Fig. 5).

As one of the essential components of shale, clay minerals have significant action on the catalysis of organic hydrocarbon generation and physically protecting OM from degradation by external agents (Kennedy et al., 2014; Berthonneau et al., 2016). With increasing thermal maturity, the evolution of clay minerals includes mainly the dehydration and microstructural change (such as reduction of interplanar spacing) (Bray et al., 1998; Bala et al., 2000), as well as the transformation of mineral type (typically smectite to illite) (Eberl et al., 1993; Metwally and Chesnokov, 2012; Chen and Xiao, 2014; Berthonneau et al., 2016). For the three shale samples, there is some smectite in T_3y and none found in S_1l and $Є_1n$ (Table 1). Possibly, the over-high maturity of S_1l and $Є_1n$ shales has transformed smectite to illite. From the FE-SEM images, clay minerals are loosely arranged and are nondirectional in T_3y (Fig. 3). However, in S_1l and $Є_1n$, accompanied by further maximum palaeoburial depths (6500 m for S_1l and 9000 m for $Є_1n$) (Liu et al., 2016), clay minerals have encountered more serious compaction, so that clay particles integrate with each other more tightly. In addition, partial clay minerals integrated with OM and formed OM-clay composites (Fig. 4 and Fig. 5). OM-clay composites have been identified as a natural source material for hydrocarbon generation, and play an important role in the enrichment and preservation of organic matter (Lu et al., 2013; Kennedy et al., 2014; Zhu et al., 2016). With the increase of maturity, the microstructure of OM-clay composites also changes. First, the composites in S_1l are less developed than $Є_1n$ and not directional, but in $Є_1n$, the composites seem to have a preferred orientational arrangement (Fig. 5d–f). With a slit-like pore geometry in OM-clay composites, it can be argued that such pores would be more prone to be compacted due to increased effective pressure as gas is drawn out of the pores (Curtis et al., 2010). Second, the boundary lines between clay minerals and OM become even more blurred with the increase of maturity, which reflects that a closer relationship between clay minerals and OM often exists in more mature samples.

To sum up, the evolution of OM and clay minerals could interplay each other. As shown in Fig. 8, with increasing maturity (from a to b and then to c), OM pores would increase at first and then

This article is protected by copyright. All rights reserved.

Accepted Article

gradually disappear, and the pores in clay minerals tend to decrease in size and number, which may be attributed to the burial and thermal histories. The evolution of OM-clay composites has a directional trend, and in over-maturity, the pores developed in the composites are more numerous than the pores in OM or clay minerals, possibly because of the protection of clay layers on the OM. Consequently, thermal maturity, as one of the most important factors to affect microstructure of OM and clay minerals, has shown great significances in the research on occurrence, preservation mechanism, and hydrocarbon generation of OM.

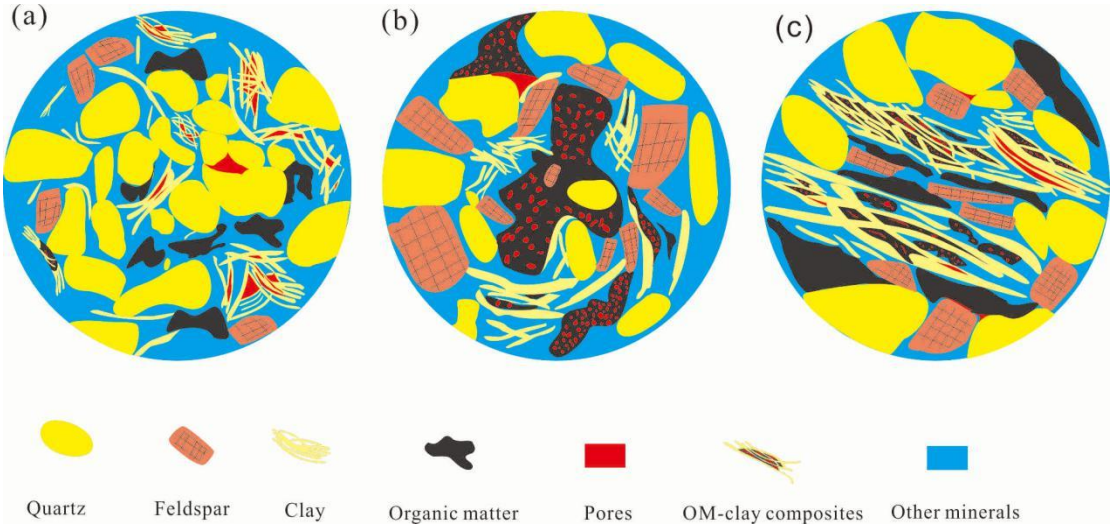

Fig. 8. Microstructure evolution of OM and clay minerals in shales with increasing thermal maturity.

(a) presents the low-mature shale (e.g., T_3y shale), (b) presents the high-mature shale (e.g., S_1l shale), and (c) presents the over-mature shale (e.g., $Є_1n$ shale).

6. Conclusions

Three representative shale samples (T_3y, S_1l, $Є_1n$) with different maturities in China were investigated to analyze the microstructure evolution of OM and clay minerals. The clay-sized samples extracted through sedimentation experiments were measured to magnify the effects of OM and clay minerals on pores. Preliminary conclusions are as follows:

(1) Both OM and clay minerals have strong effects on pore characteristics with increasing thermal maturity. For T_3y shale, clay minerals arrange loosely and develop large numbers of pores, ranging from several to hundreds of nanometers. Elliptical OM pores widespread in the S_1l shale, and are mostly in the range of mesopore to macropore. The well-developed OM-clay aggregates in $Є_1n$ shale seem to have a preferred orientation, and lots of mesopores are found in the composites.

(2) Small mesopores (2–20 nm), which developed mostly in clay minerals for T_3y, in OM for S_1l, and in OM-clay minerals for $Є_1n$ shale, are the dominant pore component among the three samples. The distribution differences of pores imply the evolutionary processes of OM and clay minerals in shale. With the increase of maturity, OM pores are absent at low maturity (T_3y) and reach the peak at high maturity (S_1l) and are destroyed or compacted at over-mature stage ($Є_1n$), and clay particles, which have gone through mineral transformation and orientational evolution, integrate with each other more tightly. The interactions of the two processes have a great significance for the microstructure evolution of OM and clay minerals in shale.

This article is protected by copyright. All rights reserved.

Accepted Article

(3) The evolution of OM and clay minerals could interplay each other, and makes the two components get closer, which is embodied in the boundaries between OM and clay minerals becoming more blurred with the sample maturity increasing. The changes of their relationship with different thermal maturity should be of great significance in the research on occurrence, preservation mechanism, and hydrocarbon generation of OM.

Acknowledgments

This work is supported by the Chinese Academy of Sciences ("Hundred Talents Program") and the National Natural Science Foundation of China (41802143).

References

Bala, P., Samantaray, B.K., and Srivastava, S.K., 2000. Dehydration transformation in Ca-montmorillonite. *Bulletin of Materials Science*, 23(1): 61–7.

Bernard, S., and Horsfield, B., 2014. Thermal maturation of gas shale systems. *Annual Review of Earth & Planetary Sciences*, 42(1), 635–651.

Berthonneau, J., Grauby, O., and Abuhaikal, M., 2016. Evolution of organo-clay composites with respect to thermal maturity in type II organic-rich source rocks. *Geochimica et Cosmochimica Acta*, 195: 68–83.

Bray, H., Redfern, S.A.T., and Clark, S.M., 1998. The kinetics of dehydration in Ca-montmorillonite: an in situ X-ray diffraction study. *Mineralogical Magazine*, 62(5): 647–56.

Chalmers, G.R.L., and Bustin, R.M., 2007. The organic matter distribution and methane capacity of the Lower Cretaceous strata of Northeastern British Columbia, Canada. *International Journal of Coal Geology*, 70(1–3): 223–239.

Chen, J., and Xiao, X.M., 2014. Evolution of nanoporosity in organic-rich shales during thermal maturation. *Fuel*, 129: 173–181.

Chen, S.B., Zuo, Z.X., Zhu, Y.M., Fu, C.Q., and Zhang, H., 2015. Applicability of the testing method for the maturity of organic matter in shale gas reservoirs. *Natural Gas Geoscience*, 26(3): 564–574 (in Chinese with English abstract).

Curtis, M.E., Ambrose, R.J., Sondergeld, C.H., and Rai, C.S., 2010. Structural characterization of gas shales on the micro- and nano-scales. SPE-137693, CSUG/SPE Canadian Unconventional Resources and International Petroleum Conference. October 19–21, 2010, Calgary, Alberta.

Curtis, M.E., Sondergeld, C.H., Ambrose, R.J., and Rai, C.S., 2012. Microstructural investigation of gas shales in two and three dimensions using nanometer-scale resolution imaging. *AAPG Bulletin*, 96(4): 665–677.

Dai, J.X., Li, J., Luo, X., Zhang,W.Z., Hu, G.Y., Ma, C.H., Guo, J.M., and Ge, S.G., 2005. Stable carbon isotope compositions and source rock geochemistry of the giant gas accumulations in the Ordos Basin, China. *Organic Geochemistry*, 36: 1617–1635.

David, T., 2013. Raman Spectroscopy of Oil Shale. *Spectroscopy*, 28(3): 20–28.

Ding, F., Cai, J.G., Song, M.S, and Yuan, P., 2013. The relationship between organic matter and specific surface area in <2 um clay size fraction of muddy source rock. *Science China: Earth Sciences*, 43(4): 634–641 (in Chinese).

Ding, W.L, Li, C., Li, C.Y., Xu, C.C., Jiu, K., and Zeng, W.T., 2012. Dominant factor of fracture development in shale and its relationship to gas accumulation. *Earth Science Frontiers*, 19(2): 212–220 (in Chinese with English abstract).

Dong, D.Z., Shi, Z.S., Sun, S.S., Guo, C.M., Zhang, C.C., Guo, W., Guan, Q.Z., Zhang, M.Q., Jiang, S., Zhang, L.F., Ma, C., Wu, J., Li, N., Chang, Y. 2018. Factors controlling microfractures in black shale: A case study of Ordovician Wufeng Formation Silurian Longmaxi Formation in Shuanghe Profile, Changning area, Sichuan Basin, SW China. *Petroleum Exploration and Development*, 45(5): 763–774.

Dong, D.Z., Wang, Y.M., Li, X.J., Zou, C.N., Guan, Q.Z., Zhang, C.C., Huang, J.L., Wang, S.F., Wang, H.Y., Liu, H.L., Bai, W.H., Liang, F., Lin, W., Zhao, Q., Liu, D.X., and Qiu, Z., 2016. Breakthrough and prospect of shale

This article is protected by copyright. All rights reserved.

Accepted Article

gas exploration and development in China. *Natural Gas Industry*, 36(1): 19–32 (in Chinese with English abstract).

Duan, Y., Wang, C.Y., Zheng, C.Y.,Wu, B.X., and Zheng, G.D., 2008. Geochemical study of crude oils from the Xifeng oilfield of the Ordos Basin, China. *Journal of Asian Earth Sciences*, 31: 341–356.

Eberl, D.D., Velde, B., and McCormick, T.,1993. Synthesis of illite-smectite from smectite at earth surface temperature and high pH. *Clay Minerals*, 28: 49–60.

Er, C., Zhao J.Z., Bai, Y.B., Fan, H., and Shen, W.X., 2013. Reservoir Characteristics of the Organic-rich Shales of the Triassic Yanchang Formation in Ordos Basin. *Oil & Gas Geology*, 34(05): 708–716 (in Chinese with English abstract).

Guo, H.J., Jia, W.L., Peng, P.A., Lei, Y.H., Luo, X.R., Cheng, M., Wang, X.Z., Zhang, L.X., and Jiang, C.F., 2014. The composition and its impact on the methane sorption of lacustrine shales from the Upper Triassic Yanchang Formation, Ordos Basin, China. *Marine and Petroleum Geology*, 57(2): 509–520.

Hartman, R.C., Ambrose, R.J., Akkutlu, I.Y., and Clarkson, C.R., 2011. Shale gas-in-place calculations Part II - Multicomponent gas adsorption effects. *SPE* 144097.

Ju, Y.W., Bu, H.L., Wang, G.C., 2014. Main characteristics of shale gas reservoir and its effect on the reservoir reconstruction. *Advances in Earth Science*, 29(4): 492–506 (in Chinese with English abstract).

Kelemen, S.R., and Fang, H.L., 2001. Maturity trends in Raman spectra from kerogen and coal. *Energy & Fuels*, 15(3): 653–658.

Kennedy, M.J., Löhr, S.C., Fraser, S.A., and Baruch, E.T., 2014. Direct evidence for organic carbon preservation as clay-organic nanocomposites in a Devonian black shale; from deposition to diagenesis. *Earth and Planetary Science Letters*, 388: 59–70.

Kuila, U., Mccarty, D.K., Derkowski, A., Fischer, T.B., Topór, T., and Prasad, M., 2014. Nano-scale texture and porosity of organic matter and clay minerals in organic-rich mudrocks. *Fuel*, 135: 359–373.

Liang, D.G., Guo, T.L., Bian, L.Z., Chen, J.P., and Zhao, Z., 2009. Some progresses on studies of hydrocarbon generation and accumulation in marine sedimentary regions, Southern China (Part 3): Controlling factors on the sedimentary facies and development of palaeozoic marine source rocks. *Marine Origin Petroleum Geology*, 14(2): 1–19 (in Chinese with English abstract).

Liu, D.H., Xiao, X.M., Tian, H., Min, Y.S., Zhou, Q., Cheng, P., and Shen, J.G., 2012. Sample maturation calculated using Raman spectroscopic parameters for solid organics: Methodology and geological applications. *China Science Bulletin*, 58(11): 1285–1298 (in Chinese).

Liu, S.G., Deng, B., Zhong, Y., Ran, B., Yong, Z.Q., Sun, W., Yang, D., Jiang, L., and Ye, Y.H., 2016. Unique geological features of burial and superimposition of the Lower Paleozoic shale gas across the Sichuan Basin and its periphery. *Earth Science Frontiers*, 23(1): 11–28 (in Chinese with English abstract).

Loucks, R.G., Reed, R.M., Ruppel, S.C., and Hammes, U., 2012. Spectrum of pore types and networks in mudrocks and a descriptive classification for matrix-related mudrock pores. *AAPG Bulletin*, 96(6): 1071–1098.

Loucks, R.G., Reed, R.M., Ruppel, S.C., and Jarvie, D.M., 2009. Morphology, genesis, and distribution of nanometer-scale pores in siliceous mudstones of the Mississippian Barnett shale. *Journal of Sedimentary Research*, 79(12): 848–861.

Lu, L.F., Cai, J.G., Liu, W.H., Tenger, and Wang, J., 2013. Occurrence and thermostability of absorbed organic matter on clay minerals in mudstones and muddy sediments, *Oil & Gas Geology*, 34 (1) :16–26 (in Chinese with English abstract).

Lu, Y.N., Zhang, J.C., Zhang, P., Huang, Y.Q., Yu, F.F., and Deng, E.D, 2015. Gas accumulation conditions of Lower Cambrian Niutitang shale and prediction of potential zones in northwestern Guizhou. *Marine Origin Petroleum Geology*, 20(2): 37–44 (in Chinese with English abstract).

Metwally, Y.M., Chesnokov, E.M., 2012. Clay mineral transformation as a major source for authigenic quartz in thermo-mature gas shale. *Applied Clay Science*, 55: 138–50.

Romero-Sarmiento, M. F., Rouzaud, J. N., Bernard, S., Deldicque, D., Thomas, M., and Littke, R., 2014. Evolution of barnett shale organic carbon structure and nanostructure with increasing maturation. *Organic Geochemistry*, 71(6): 7–16.

Rouquerol, J., Avnir, D., Fairbridge, C.W., Everett, D.H., Haynes, J.H., Pernicone, N., Ramsay, J.D.F., Sing, K.S.W., and Unger, K.K., 1994. Recommendations for the characterization of porous solids. *Pure and Applied Chemistry*, 66(08): 1739–1758.

Schoenherr, J., Littke, R., Urai, J.L., Kukla, P.A., and Rawahi, Z., 2007. Polyphase thermal evolution in the Infra-Cambrian Ara Group (South Oman Salt Basin) as deduced by maturity of solid reservoir bitumen. *Organic Geochemistry*, 38(8): 1293–1318.

This article is protected by copyright. All rights reserved.

Accepted Article

Sing, K.S.W., Everett, D.H., Haul, R.A.M., Moscou, L., Pierotti, R.A., Rouquerol, J., Siemieniewska, T., 1985. Physical and biophysical chemistry division commission on colloid and surface chemistry including catalysis. *Pure and Applied Chemistry*, 57(603): 1–6.

Slatt, R.M., and O'Brien, N.R., 2011. Pore types in the Barnett and Woodford gas shales: Contribution to understanding gas storage and migration pathways in fine-grained rocks. *AAPG Bulletin*, 95(12): 2017–2030.

Tan, L.Y., Xu, Y., Li, D.H., Cheng, L.J., Zeng, C.L., 2015. Geological condition of shale gas accumulation and favorable area prediction for the Wufeng-Longmaxi Formatioins in Southeastern Chongqing. Acta Geologica Sinica, 89(7): 1308–1317 (in Chinese with English abstract).

Tang, X., Zhang, J., Jin, Z., Xiong, J., Lin, L., Yu, Y., and Han, S., 2015. Experimental investigation of thermal maturation on shale reservoir properties from hydrous pyrolysis of Chang 7 shale, Ordos Basin. *Marine and Petroleum Geology*, 64: 165–172.

Wang, P., Jiang, Z., Chen, L., Yin, L., Li, Z., Zhang, C., Tang, X., and Wang, G., 2016. Pore structure characterization for the Longmaxi and Niutitang shales in the Upper Yangtze Platform, South China: Evidence from focused ion beam He ion microscopy, nano-computerized tomography and gas adsorption analysis. *Marine and Petroleum Geology*. 77: 1323–1337.

Yang, F., Ning, Z.F., Wang, Q., and Liu, H.Q., 2016a. Pore structure of Cambrian shales from the Sichuan Basin in China and implications to gas storage. *Marine and Petroleum Geology*, 70: 14–26.

Yang, H., Niu, X.B., Xu, L.M., Feng, S.B., You, Y., Liang, X.W., Wang, F., Zhang, D.D., 2016b. Exploration potential of shale oil in Chang7 Member, Upper Triassic Yanchang Formation, Ordos Basin, NW China. *Petroleum Exploration and Development*, 43(4): 511–520 (in Chinese with English abstract).

Yang, P., Wang, Z.J., Xie, Y., Du, Q.D., Chen, H.G., and He, Y.Z., 2012. The biomarker characteristics and sedimentary environment of Early Cambrian Niutitang Formation source rock in northern Guizhou. *Geological Bulletion of China*, 31(11): 1910–1921 (in Chinese with English abstract).

Yuan, X.J., Lin, S.H., Liu, Q., Yao, J.L., Wang, L., Guo, H., Deng, X.Q, and Cheng, D.W., 2015. Lacustrine fine-grained sedimentary features and organic-rich shale distribution pattern: A case study of Chang 7 Member of Triassic Yanchang Formation in Ordos Basin, NW China. *Petroleum Exploration and Development*, 42(1): 34–43 (in Chinese with English abstract).

Zhang, C.M., Zhang, W.S., Guo, Y.H., 2012. Sedimentary environment and its effect on hydrocarbon source rocks of Longmaxi Formation in southeast Sichuan and northern Guizhou. *Earth Science Frontiers*, 19(1): 136–145 (in Chinese with English abstract).

Zhao, J.H., Jin, Z.J., Jin, Z.K., Wen, X., Geng, Y.K., Yan, C.N., and Nie, H.K., 2016. Lithofacies types and sedimentary environment of shale in Wufeng-Longmaxi Formation, Sichuan Basin. *Acta Petrolei Sinica*, 37(5): 572–586 (in Chinese with English abstract).

Zhu, X.J., Cai, J.G., Liu, W.X., and Lu, X.C., 2016. Occurrence of stable and mobile organic matter in the clay-sized fraction of shale: Significance for petroleum geology and carbon cycle. *International Journal of Coal Geology*, 160–161: 1–10.

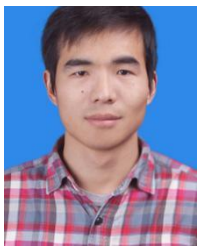

About the first author

GU Yuantao, male, born in 1990 in Luoyang City, Henan Province; PhD; graduated from Institute of Geochemistry, Chinese Academy of Sciences; lecturer of Henan University of Engineering. He is now interested in the study on shale gas reservoirs. Email: guyuantao@haue.edu.cn; phone: 13027620089.

About the corresponding author

WAN Quan, male, born in 1971 in Luzhou City, Sichuan Province; PhD; graduated from State University of New York at Stony Brook; professor of Institute of Geochemistry, Chinese Academy of Sciences. He is now interested in nanogeochemistry. Email: wanquan@vip.gyig.ac.cn; phone:13985849480.

This article is protected by copyright. All rights reserved.